Faraday Discussions

Cite this: *Faraday Discuss.*, 2019, **214**, 175

PAPER

Carrier dynamics and spin–valley–layer effects in bilayer transition metal dichalcogenides

Christopher J. Ciccarino,[ab] Chitraleema Chakraborty,[ac] Dirk R. Englund[c] and Prineha Narang *[a]

Received 26th October 2018, Accepted 26th November 2018
DOI: 10.1039/c8fd00159f

Transition metal dichalcogenides are an interesting class of low dimensional materials in mono- and few-layer form with diverse applications in valleytronic, optoelectronic and quantum devices. Therefore, the general nature of the band-edges and the interplay with valley dynamics is important from a fundamental and technological standpoint. Bilayers introduce interlayer coupling effects which can have a significant impact on the valley polarization. The combined effect of spin–orbit and interlayer coupling can strongly modify the band structure, phonon interactions and overall carrier dynamics in the material. Here we use first-principles calculations of electron–electron and electron–phonon interactions to investigate bilayer MoS_2 and WSe_2 in both the AA′ and AB stacking configurations. We find that in addition to spin–orbit coupling, interlayer interactions present in the two configurations significantly alter the near-band-edge dynamics. Scattering lifetimes and dynamic behavior are highly material-dependent, despite the similarities and typical trends in TMDCs. Additionally, we capture significant differences in dynamics for the AA′ and AB stacking configurations, with lifetime values differing by up to an order of magnitude between them for MoS_2. Further, we evaluate the valley polarization times and find that maximum lifetimes at room temperature are of the scale of 1 picosecond for WSe_2 in the AB orientation. These results present a pathway to understanding complex heterostructure configurations and 'magic angle' physics in TMDCs.

I. Introduction

Transition metal dichalcogenides (TMDCs) have been extensively studied in monolayer and few-layer forms for a variety of both fundamental and technological reasons. In the monolayer, TMDCs have been shown to be of optical

[a]*John A. Paulson School of Engineering and Applied Sciences, Harvard University, Cambridge, MA, USA. E-mail: prineha@seas.harvard.edu*
[b]*Department of Chemistry and Chemical Biology, Harvard University, Cambridge, MA, USA*
[c]*Department of Electrical Engineering and Computer Science, Massachusetts Institute of Technology, Cambridge, MA, USA*

interest due to their efficient emission properties as direct band-gap semiconductors.[1–3] Additionally, spin-selective excitation is possible using circularly polarized light,[4] enabling controlled valley population. Without an inversion center, spin and valley pseudospin can couple, leading to the spin–valley locking phenomena useful in valleytronic applications such as information processing.[5–7]

Bilayer TMDCs are compelling in a host of unique ways;[8] multilayer stacks of TMDCs interact with neighboring layers *via* van der Waals interactions. These weak interactions allow for the possibility of fabricating multilayer stacks with controllable precision in orientation and ordering.[9–11] Unique material phenomena have already been found using this stacking degree of freedom, including superconductivity in graphene[12] and band-gap tuning in heterostructure TMDCs,[13–15] for example. In general, control of interlayer twist angles can introduce long range Moiré patterns, effectively acting as a long range potential modulator. Moiré effects have been previously studied in bilayer MoS_2, which introduced novel phonon modes associated with long-range periodicity.[16] Theoretical studies have also investigated the effects of strain and its relation to interlayer coupling using tight-binding methods.[17–19] Interlayer coupling effects have shown modulation of photoluminescence[20] and more recently have been demonstrated to introduce relaxation pathways for excited carriers in heterostructures.[21] More fundamentally, band-edge states have been shown to be sensitive to interlayer coupling effects.[22] TMDC heterostructures have also been demonstrated to have ultra long valley polarization times in experiment.[23]

These interesting experimental demonstrations motivate our work towards a thorough, fundamental understanding of the physics in multilayer TMDC systems. In the bilayer, TMDCs are indirect band-gap materials, similar in this way to their bulk behavior.[24] Despite this, these systems retain interest from the valleytronic community for a number of reasons, including the fact that their inversion symmetry can be tuned by electric fields,[25] and have overall been more susceptible to electric field manipulation than monolayers.[26] Additionally, strong valley polarization has been observed in bilayer WS_2[27] due to spin–orbit splitting. Understanding valleytronic applicability in these systems requires a detailed understanding of the band structure and phonon properties of the material.

Overall, the dynamics of bilayer TMDCs present a substantial theoretical and computational challenge relative to their monolayer counterparts. The effects of interlayer coupling must be considered, which strongly influences the band edge states. Additionally, stacking orientation is paramount to understanding the symmetry of the system, which can severely affect valley dynamics through spin–orbit coupling. The experimentally observed AA′ (also known as the 2H phase) and AB (also known as the 3R phase) orientations of bilayer TMDCs[28,29] introduce differences in interlayer coupling and symmetries, which can induce unique material behavior. In the bilayer, spin and valley pseudospin degrees of freedom can additionally couple to the layer index, denoted as layer pseudospin, such that all three of these quantum numbers describe the K point valleys of the system.[30] Here, opposite spins from opposite layers are coupled at each of the split valence bands, such that transitions must consider interlayer hopping as well as spin flipping. Additionally, different stacking configurations can lead to shifts in phonon frequencies, spin–orbit splitting and the magnitude of van der Waals

interactions.[31] All of these effects create a complicated system compared to the monolayer case and require new theoretical and computational implementations.

In this work, we present a novel *ab initio* approach for electron–electron and electron–phonon interactions to study bilayer MoS_2 and WSe_2 systems in both the AA′ and AB stacking orientations. We compare our self-consistent spin–orbit calculated dynamics with spin-degenerate calculations in order to understand the impact of spin–orbit coupling on dynamics in these systems. Importantly, we find that in both materials, a detailed understanding of spin–orbit splitting, interlayer coupling and symmetry effects is required in order to understand the different dynamics captured for each of the material configurations. Further, we find that spin–orbit effects are more relevant in WSe_2 due to its larger spin-splitting, while the smaller splitting in MoS_2 has a much weaker effect on dynamics. This is in contrast with the uniform TMDC trends seen in monolayers.[32] Additionally, we calculate hot carrier profiles and find that despite the indirect nature of all the systems considered, direct transitions dominate the calculated results, in qualitatively excellent agreement with the optical properties observed experimentally. These results provide a pathway for future studies in TMDC dynamics, including heterostructures, twisted bilayer 'magic angle' physics, and larger multilayer stacks.

II. Methods

All calculations were performed using JDFTx,[33] based on density-functional theory (DFT). We model the bilayers using PBEsol[34] pseudopotentials for a plane-wave basis set with a 25 hartree energy cutoff on a $9 \times 9 \times 1$ reciprocal space grid. To describe the bilayer effectively, we employ the Grimme D2 correction for interlayer coupling[35] as well as Coulomb truncation[36] in the out-of-plane direction, such that periodic images of the bilayer are neglected. Phonons are calculated using the frozen phonon approach on a $3 \times 3 \times 1$ supercell. In relativistic calculations, spin–orbit coupling is self-consistently included, distinct from previous work in these materials. Each cell was relaxed and the a lattice constant found to agree with experiment to within 1%. The interlayer spacing of the AB-stacked MoS_2 (WSe_2) bilayer corresponds well with the out-of-plane lattice constant of 12.27 Å (12.98 Å), which is within 1% of the bulk lattice value in each material. The AA′ configuration showed a 10% reduction in the interlayer spacing for both MoS_2 and WSe_2.

In order to effectively capture the dynamical properties of the system, a dense sampling of $\mathbf{k}$ points in the Brillouin zone (BZ) is required. Conventional DFT approaches to generating these meshes are inadequate given the computational cost. Instead, we employ a Wannier function scheme which describes the Bloch space Kohn–Sham states on an equivalent real space grid.[37] We can then transform back to reciprocal space on a finely-spaced grid of $\mathbf{k}$ points. This enables efficient, high-fidelity BZ sampling, crucial for our calculations. In the calculations presented, Wannier interpolation allows us to sample $\sim 10^6$ $\mathbf{k}$ points in the 2D BZ of the bilayer. We apply these interpolation methods in calculations which both omit and include spin–orbit coupling, where the latter employs spinorial trial functions to explicitly include spin. Trial centers are made up of transition metal d orbitals and chalcogen p orbitals for capturing bands nearest to the band gap.

III. Results and discussion

A. Electronic structure

It is useful to first consider the monolayer band structure before considering the bilayer. In the monolayer, spin–orbit coupling alone accounts for significant splitting of the valence band at the *K* point and the conduction band at the *Q* point. In conjunction with the lack of an inversion center, it is relatively easy to understand the origin of the splitting in these systems. In the bilayer case, especially when considering the multiple possible stacking configurations, corresponding symmetry and interlayer coupling effects can introduce complications in addition to spin–orbit coupling. Symmetry plays a pivotal role in understanding how spin–orbit splitting impacts the band structure, while interlayer coupling has already been shown to most strongly affect bands near the band edges.[22] Together these interactions promise to have important effects on the scattering possibilities of a given system.

The calculated spin–orbit split band structures of each of the bilayer orientations are plotted in Fig. 1. Despite the weak van der Waals forces governing interlayer interactions, the states near the band edge are clearly affected by interlayer coupling to some degree.[22,38] These states are composed of mostly d orbitals from the transition metal atom, where the *K* point of the valence band and the *Q* point of the conduction band are both comprised of the $d_{x^2-y^2}$ and d_{xy} orbitals which introduce significant splitting.[39] In the AA′ case, a combination of

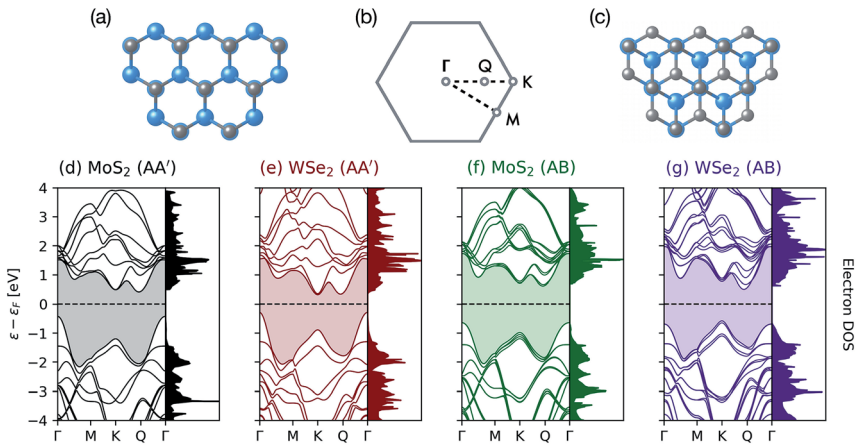

Fig. 1 Bilayer TMDC structure, orientation and electronic structure. Panels (a) and (c) show the stacking arrangement of the two TMDC layers in the out-of-plane direction for the AA′ and AB orientations, respectively. The band structures in panels (d)–(g) are plotted along the high-symmetry lines defined by the two dimensional Brillouin zone depicted in panel (b). The conduction band edge states in all cases are at the *K* and *Q* points, whereas the valence band edges are at the *K* and *Γ* points. All four of these points are sensitive to interlayer coupling, and the *Q* of the conduction band and *K* of the valence band are split further by a combination of spin–orbit and interlayer coupling. In the AA′ orientation the primary splitting is a result of interlayer coupling, while in the AB orientation it is the spin–orbit effects which introduce large splitting values. The smaller overall band gap of the AA′ orientation is suggestive of stronger interlayer coupling, as the predicted interlayer spacing for these layers is 10% smaller than the spacing in the AB configuration.

the out-of-plane interlayer coupling and intralayer spin–orbit splitting introduces sizable splits in the observed valence band edge at the *K* point (up to 550 meV in WSe_2). However, only two energetically distinct valleys are observed, which is a direct result of inversion symmetry. This configuration represents the spin–valley–layer locking state, where each valley is composed of opposite spin states for opposite layers of the TMDC,[30] which together can be indexed by the spin, valley pseudospin and layer pseudospin index. In the AB configuration, four non-degenerate valleys emerge due to the lack of an inversion center. Interestingly, the stacking orientation also impacts the interlayer spacing, suggesting orientation-dependent van der Waals interactions. For both MoS_2 and WSe_2, the interlayer spacing decreased by ~10% for the AA′ configurations relative to the AB configuration. This, as previously investigated and confirmed in our results, leads to blue-shifted phonon modes in addition to impacting the interlayer coupling effects on the electronic structure.[31]

The confluence of spin–orbit and interlayer coupling effects on the splitting in the band structure is distinct for the AA′ and AB stacking configurations. In the AA′ stacking, the splitting of the valence band at the *K* point is substantial, even in the spin-degenerate calculations. This suggests that splitting of the *K* valley is dominated by interlayer coupling effects. When spin–orbit effects are included, these splits then increase further, but there is no additional splitting of the two bands into four: this is forbidden in the inversion-symmetric cell. However, in the AB configuration, the splitting from interlayer coupling alone is considerably smaller. Instead, the observed splittings seen in Fig. 1(f and g) are primarily due to spin–orbit coupling effects. This correlates well with the larger interlayer spacing found in the AB-stacked cells, which indicates weaker interlayer interactions. The spin–orbit splitting mechanism which dominates the splitting in the AB orientation is important when understanding possible electronic transitions.

B. Lifetimes

In determining the total scattering rate for carriers, we consider Coulomb scattering between two electrons (e–e) as well as electron–phonon (e–ph) scattering. Together, these processes contribute to the total scattering rate, given by Matthiessen's rule:

$$\tau_{\mathbf{k}n}{}^{-1} = (\tau_{\mathbf{k}n}^{\mathrm{e-e}})^{-1} + (\tau_{\mathbf{k}n}^{\mathrm{e-ph}})^{-1}, \tag{1}$$

which is indexed by a carrier in band n and wave-vector $\mathbf{k}$ in the two-dimensional Brillouin zone. Each of these processes are modeled using a diagrammatic framework, where we compute the contribution of each process to the electronic self-energy $\Sigma_{\mathbf{k}n}$ as described formally in a field theoretic approach. Thus, in general the lifetime is given by $\tau_{\mathbf{k}n}^{\mathrm{e-e(e-ph)}} = \hbar/2\Sigma_{\mathbf{k}n}^{\mathrm{e-e(e-ph)}}$. The Coulomb-mediated electron scattering is therefore written as:[40]

$$\left(\tau_{\mathbf{k}n}^{\mathrm{e-e}}\right)^{-1} = \frac{2\pi}{\hbar}\int_{\mathrm{BZ}}\frac{\mathrm{d}\mathbf{k}'}{(2\pi)^2}\sum_{n'}\sum_{\mathbf{G}\mathbf{G}'}\tilde{\rho}_{\mathbf{k}'n',\mathbf{k}n}(\mathbf{G})\tilde{\rho}^{*}_{\mathbf{k}'n',\mathbf{k}n}\left(\mathbf{G}'\right)\times\frac{1}{\pi}\ \mathrm{Im}\ W_{\mathbf{G}\mathbf{G}'}\left(\mathbf{k}'-\mathbf{k},\varepsilon_{\mathbf{k}n}-\varepsilon_{\mathbf{k}'n'}\right). \tag{2}$$

Here we employ the single-particle electronic density matrices $\tilde{\rho}_{\mathbf{k}'n',\mathbf{k}n}(\mathbf{G})$ and capture the imaginary part of their interaction *via* the dynamically screened Coulomb interaction, $W_{\mathbf{GG}'}(\mathbf{k}' - \mathbf{k},\omega)$, which is evaluated within the random phase approximation. This calculation is performed in the plane-wave basis of reciprocal lattice vectors $\mathbf{G}$ and $\mathbf{G}'$, and involves a sum over a full second set of electronic states ($\mathbf{k}'n'$).

The electron–phonon lifetime is determined using Fermi's Golden rule:

$$\left(\tau_{\mathbf{k}n}^{\mathrm{e-ph}}\right)^{-1} = \frac{2\pi}{\hbar}\sum_{n'\alpha\pm}\int_{\mathrm{BZ}}\frac{\Omega \mathrm{d}\mathbf{k}'}{(2\pi)^2}\delta\left(\varepsilon_{\mathbf{k}'n'} - \varepsilon_{\mathbf{k}n} \mp \hbar\omega_{\mathbf{q}\alpha}\right) \times \left[n_{\mathbf{q}\alpha} + \frac{1}{2} \mp \left(\frac{1}{2} - f_{\mathbf{k}'n'}\right)\right]\left|g_{\mathbf{k}'n',\mathbf{k}n}^{\mathbf{q}\alpha}\right|^2. \quad (3)$$

In this expression, final electronic bands n' and phonon polarizations α are summed over while integration is performed over the entire 2D BZ. The δ function imposes energy conservation for all scattering processes involving initial (final) electronic states $\mathbf{k}n$ ($\mathbf{k}'n'$) with corresponding energies $\varepsilon_{\mathbf{k}n}$ ($\varepsilon_{\mathbf{k}'n'}$) and a phonon in

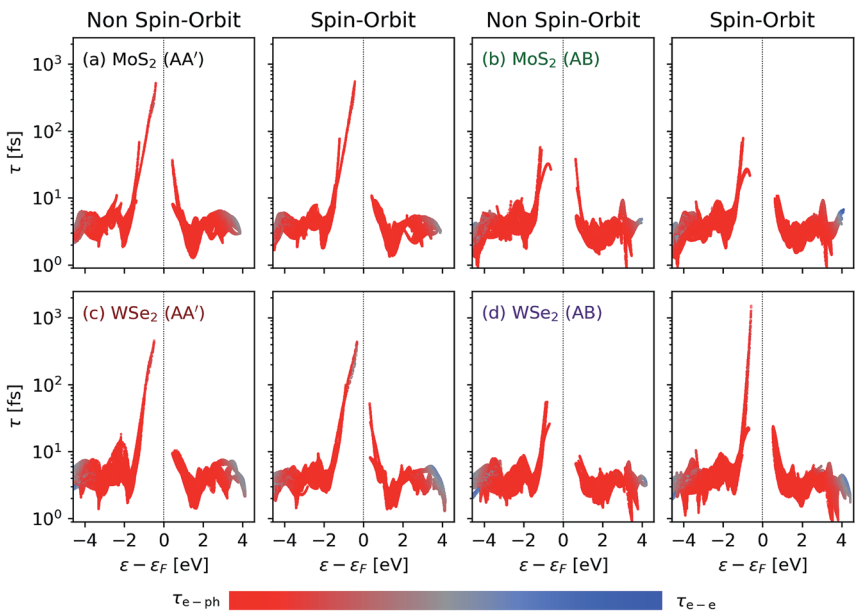

Fig. 2 (a–d) Calculated scattering lifetimes in each of the bilayer TMDCs studied. The lifetimes in the AA′ and AB configurations are relatively similar except at the band edges. The hole lifetimes of both TMDCs are not significantly affected by spin–orbit splitting in the AA′ configuration, as the effect of spin–orbit coupling is to increase the already-split valence band edge, which is induced by interlayer coupling. Electron lifetimes are increased in WSe_2 with spin and decreased in MoS_2 with spin because of the relative energies of the Q and K valleys. Spin–orbit coupling pushes the Q point to phonon-accessible energies relative to the K point in MoS_2, while it pushes the Q valley away from the K valley in the case of WSe_2. In the AB configuration, hole lifetimes of WSe_2 are found to significantly increase as a result of spin–orbit coupling, while hole lifetimes in MoS_2 are predicted to be relatively unaffected. Similar to the AA′ configuration, electron lifetime trends are governed by the relative energies of the Q and K valleys. The relative contribution of electron–electron and electron–phonon interactions to the lifetime is indicated by the color bar. All scattering observed is dominated by electron–phonon processes.

state $\mathbf{q}\alpha$ with energy $\hbar\omega_{\mathbf{q}\alpha}$. Diagrammatically this represents a three-vertex. The $\mp$ accounts for both phonon emission and absorption. These scattering events are weighted by the phononic (Bose) and electronic (Fermi) occupation factors described by $n_{\mathbf{q}\alpha}$ and $f_{\mathbf{k}n}$, respectively. Finally, the electron–phonon matrix element which describes the coupling of these two electronic states with the phonon mode is denoted by $g^{\mathbf{q}\alpha}_{\mathbf{k}'n',\mathbf{k}n}$. We note that in order to satisfy conservation of crystal momentum, $\mathbf{q} = \mathbf{k}' - \mathbf{k}$ for all terms which contribute to the above expression. We interpolate our DFT-based couplings using Wannier functions to generate an ultra-fine mesh of matrix elements for converged integration.

After solving for each lifetime individually, the total scattering lifetimes are determined from eqn (1) and presented in Fig. 2. As seen in the figure, the scattering within 4 eV of the Fermi energy is dominated by electron–phonon interactions. The AA′ stacking configuration shows that spin–orbit coupling has a negligible impact on the hole lifetime at the valence band edge. This is because the band structures even in the spin-degenerate calculations are sufficiently split by interlayer coupling,[22] with splitting values of 165 meV for MoS_2 and 240 meV for WSe_2. We note that the maximum phonon energy for these systems is 60 meV, thus scattering between each of these valleys is not accessible, enabling long-lived states. Introducing spin–orbit splitting indeed increases the splitting values by about 60 meV (310 meV) in MoS_2 (WSe_2), but this does not change the dynamics any further. Meanwhile excited electrons at the conduction band edge are slightly affected by spin–orbit coupling, however, the effect is opposite for each TMDC. In MoS_2, lifetimes decrease with spin–orbit coupling, as this shifts the Q point towards K for more energetically accessible K–Q scattering, while the opposite occurs in WSe_2: the energy separation between the Q and K valleys becomes larger.

The results in the AB configuration are equally interesting and material-dependent. Hole dynamics in MoS_2 are hardly affected by spin–orbit coupling, while electron lifetimes are again decreased for the same Q-related reason as in the AA′ scenario. Meanwhile, hole lifetimes in WSe_2 are significantly enhanced when spin–orbit coupling is introduced, similar to the behavior observed in monolayer systems. In this case, the larger splitting induced by WSe_2 relative to MoS_2 is sufficient to shrink the phase space for electron–phonon scattering. In the AB configuration, spin–orbit coupling pushes the valence band edge of WSe_2 to the energetically-isolated K point, whereas the band edge in MoS_2 is still the Γ point. The spin–orbit-induced shift of the K point valence band removes possible K–Γ electron–phonon scattering and therefore enhances hole lifetimes, which are clearly very sensitive to band-edge position.

In general, the spin-related effects on dynamics are opposite for the MoS_2 and WSe_2 systems, which is distinctly different from the behavior observed for monolayer TMDCs.[32] In addition, the magnitude of the lifetimes are at least 50% lower than the corresponding monolayer case, regardless of spin considerations. The maximum valley coherence time calculated at room temperature is only 1 picosecond in WSe_2, which is 4 times smaller than the time determined for the same monolayer system.[32] However, hole lifetimes are still observed to be larger than electron lifetimes in general, consistent with the trends in the monolayer case. The bilayer structures can be said to introduce more scattering channels than the monolayer case, given that the band edge is not isolated at K in many of the systems studied. van der Waals effects *via* interlayer coupling have previously been shown to have an impact on predicted dynamics.[41] The nature of the band edges (especially

compared to the monolayer case) are crucial to explain the smaller lifetimes predicted for the TMDCs studied. Additionally, the alignment of the layers and their corresponding symmetries impact the nature and strength of interlayer and spin–orbit coupling, which manifests in the substantially different dynamics observed, as is visible when comparing the left- and right-hand side of Fig. 2.

C. Mobility

In addition to lifetimes, we can also evaluate the predicted carrier mobilities, which are also governed by electron–phonon interactions. Using the same general formalism used in eqn (3), we compute the momentum-relaxing lifetimes $\tau^{\mathrm{p}}_{\mathbf{k}n}$ by accounting for the angle between the electron velocities before and after scattering. This is given by:

$$\left(\tau^{\mathrm{p}}_{\mathbf{k}n}\right)^{-1} = \frac{2\pi}{\hbar}\sum_{n'\alpha\pm}\int_{\mathrm{BZ}}\frac{\Omega \mathrm{d}\mathbf{k}'}{(2\pi)^2}\delta\left(\varepsilon_{\mathbf{k}'n'} - \varepsilon_{\mathbf{k}n} \mp \hbar\omega_{\mathbf{q}\alpha}\right) \times \left[n_{\mathbf{q}\alpha} + \frac{1}{2} \mp \left(\frac{1}{2} - f_{\mathbf{k}'n'}\right)\right]\left|g^{\mathbf{q}\alpha}_{\mathbf{k}'n',\mathbf{k}n}\right|^2 \times\left(1 - \frac{\mathbf{v}_{\mathbf{k}n}\cdot\mathbf{v}_{\mathbf{k}'n'}}{\left|\mathbf{v}_{\mathbf{k}n}\right|\left|\mathbf{v}_{\mathbf{k}'n'}\right|}\right), \quad (4)$$

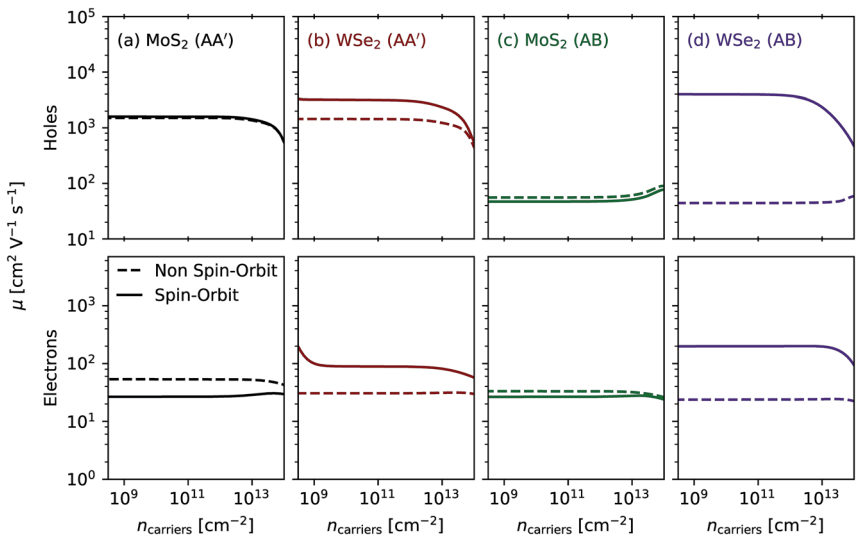

Fig. 3 (a–d) Calculated mobilities of AA′ and AB-stacked transition metal dichalcogenides. In general, the spin–orbit interactions more significantly affect the mobilities in WSe_2 than in MoS_2, which is a result of its larger predicted splitting and the relative energies of the valleys at each of the band edges. Both the AA′ and AB configurations of WSe_2 show increased mobilities with spin–orbit coupling for the hole and electron cases. Similarly to the lifetime in Fig. 2, the AB orientation introduces a larger difference between spin–orbit and non spin–orbit predictions than AA′, where there is over an order of magnitude increase for the same reasons described for Fig. 2. Compared to calculated monolayer mobilities, both configurations of the TMDCs have mobilities smaller than those of their monolayer counterparts, except in the case of the electron mobility of AB-stacked WSe_2, which is slightly larger in the bilayer compared to the monolayer when spin–orbit interactions are considered.

which is identical to eqn (3) except for the angular dependence, denoted by the band velocities $\mathbf{v}_{\mathbf{k}n}$ (defined as $\mathbf{v} \equiv \partial\varepsilon/\partial\mathbf{k}$) of the initial $\mathbf{k}n$ and final $\mathbf{k}'n'$ states. After calculating $\tau^{\mathrm{p}}_{\mathbf{k}n}$, we determine the mobility by solving the linearized Boltzmann equation using a full-band relaxation-time approximation:

$$\overline{\mu}(\varepsilon_{\mathrm{F}}) = \frac{e}{|n(\varepsilon_{\mathrm{F}})|}\sum_{n}\int_{\mathrm{BZ}}\frac{g_{\mathrm{s}}\mathrm{d}\mathbf{k}}{(2\pi)^2}\frac{\partial f_{\mathbf{k}n}(\varepsilon_{\mathrm{F}})}{\partial\varepsilon_{\mathbf{k}n}}(\mathbf{v}_{\mathbf{k}n}\otimes\mathbf{v}_{\mathbf{k}n})\tau^{\mathrm{p}}_{\mathbf{k}n}. \quad (5)$$

Here g_{s} is the spin degeneracy of the band (=1 with and =2 without spin–orbit coupling). The derivative of the Fermi function effectively selects carriers which contribute to transport at a specified doping level given as ε_{F}. We further define the density $n(\varepsilon_{\mathrm{F}})$ for a given Fermi energy as:

$$n(\varepsilon_{\mathrm{F}}) = \sum_{n}\int_{\mathrm{BZ}}\frac{g_{\mathrm{s}}\mathrm{d}\mathbf{k}}{(2\pi)^2}f_{\mathbf{k}n}(\varepsilon_{\mathrm{F}}) - n_0. \quad (6)$$

This quantity is positive for n-type semiconductors and negative for p-type semiconductors. The quantity n_0 represents the number density of carriers in the neutral DFT calculation.

Using this formalism, we vary the Fermi-level and evaluate eqn (4)–(6) in order to determine the mobility as plotted in Fig. 3. Similarly to the lifetime behavior observed, the role of spin–orbit coupling in the predicted mobilities is systematically different when comparing MoS_2 and WSe_2 for both the AA′ and AB stacking configurations. The mobilities are similar for electrons and holes in these regions, and spin reduces the electron mobility in both stacking configurations. On the other hand, the mobility in WSe_2 is highly dependent on spin–orbit coupling for both electrons and holes. In the hole case, spin-splitting isolates the K point from Γ at the valence band edge, while in the electron case it isolates Q from K, both cases helping to remove scattering channels and improve mobility. The enhanced electron mobility is novel from the monolayer results, as here the Q point is energetically more separated from K than it was in the monolayer. Despite this, all of these calculated mobilities are smaller than those predicted in the monolayer. The only slight exception to this is the electron mobility in the AB configuration of WSe_2, which is slightly larger than that in the monolayer when spin–orbit coupling effects are included.

D. Hot carriers

Information about electron–electron and electron–phonon coupling allows us to better understand the optical response. This is especially important for TMDCs, which are efficient sources of long-lived inter-layer excitons[42] and single photon emitters[43–46] exhibiting widely tunable properties when embedded in multilayer heterostructures.[20,47,48] While we do not explicitly account for excitonic effects in our calculations, these results hint at the importance of direct transitions, and our calculated response can provide a qualitative understanding of the nature of favorable excitation pathways. We calculate the complex dielectric function for each monolayer by including both direct and phonon-assisted transitions:

$$\overline{\varepsilon}(\omega) = \overline{\varepsilon}_{\mathrm{direct}}(\omega) + \overline{\varepsilon}_{\mathrm{phonon}}(\omega). \quad (7)$$

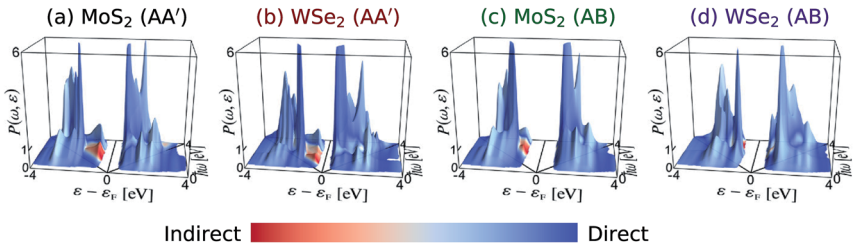

Fig. 4 (a–d) Hot carrier generation profiles of AA′ and AB-stacked transition metal dichalcogenides. The profiles are normalized and show the likelihood of hot carriers being generated from direct *vs.* indirect transitions. In all cases, despite the indirect nature of the band gap, transitions are dominated by direct transitions as opposed to indirect. This is an interesting yet surprising result from our calculations. The indirect transitions at the valence band edge suggest that Γ valleys can be populated, but their overall density of states limits the quantity of transitions to this energy. Meanwhile, direct transitions associated with the K point dominate the hot carrier generation mechanisms for the photon energy range considered.

Fermi's Golden rule is used to calculate the imaginary part of the direct contribution *via*:[49]

$$\hat{\boldsymbol{\lambda}}\cdot \mathrm{Im}\,\bar{\varepsilon}_{\mathrm{direct}}(\omega)\cdot\hat{\boldsymbol{\lambda}} = \frac{4\pi^2 e^2}{\omega^2}\int_{\mathrm{BZ}}\frac{\mathrm{d}k}{(2\pi)^2}\sum_{n'n}\left(f_{kn}-f_{kn'}\right)\times\delta\left(\varepsilon_{kn'}-\varepsilon_{kn}-\hbar\omega\right)\left|\hat{\boldsymbol{\lambda}}\cdot\mathbf{v}^{\mathbf{k}}_{n'n}\right|^2, \tag{8}$$

which describes electronic transitions from initial and final electronic states which involve a photon of energy $\hbar\omega$. The variable $\hat{\boldsymbol{\lambda}}$ is a test unit vector oriented in the same direction as the field, which enables for directionally-dependent characterization of the dielectric response. We capture the response from a field oriented perpendicular to the bilayer. Indirect transitions can also contribute to optical excitation and hot carrier generation. In order to evaluate the electron–phonon scattering involved in these processes, the phonon-assisted process is captured using second-order perturbation theory:[50]

$$\begin{aligned}\hat{\boldsymbol{\lambda}}\cdot \mathrm{Im}\,\bar{\varepsilon}_{\mathrm{phonon}}(\omega)\cdot\hat{\boldsymbol{\lambda}} = \frac{4\pi^2 e^2}{\omega^2}\int_{\mathrm{BZ}}\frac{\mathrm{d}\mathbf{k}'\mathrm{d}\mathbf{k}}{(2\pi)^4}\sum_{n'n\alpha\pm}&\left(f_{\mathbf{k}n}-f_{\mathbf{k}'n'}\right)\\ &\times\left(n_{\mathbf{q},\alpha}+\frac{1}{2}\mp\frac{1}{2}\right)\delta\left(\varepsilon_{\mathbf{k}'n'}-\varepsilon_{\mathbf{k}n}-\hbar\omega\mp\hbar\omega_{\mathbf{q},\alpha}\right)\\ &\times\left|\hat{\boldsymbol{\lambda}}\cdot\sum_{n_1}\left(\frac{g^{\mathbf{q},\alpha}_{\mathbf{k}'n',\mathbf{k}n_1}\mathbf{v}^{\mathbf{k}}_{n_1 n}}{\varepsilon_{\mathbf{k}n_1}-\varepsilon_{\mathbf{k}n}-\hbar\omega+\mathrm{i}\eta}+\frac{\mathbf{v}^{\mathbf{k}'}_{n'n_1}g^{\mathbf{q},\alpha}_{\mathbf{k}'n_1,\mathbf{k}n}}{\varepsilon_{\mathbf{k}'n_1}-\varepsilon_{\mathbf{k}n}\mp\hbar\omega_{\mathbf{q},\alpha}+\mathrm{i}\eta}\right)\right|^2.\end{aligned} \tag{9}$$

Here all symbols are as they have previously been defined, and once more the summation over $\pm$ ensures that both phonon emission and absorption processes are captured. The δ-function ensures energy conservation if broadened to Lorentzians whose widths are related to the initial and final carrier linewidths, and the η quantity is to ensure singular contributions are eliminated. These quantities

are again evaluated on a dense BZ grid generated *via* our *ab initio* Wannier function techniques.

By calculating these quantities we capture the relative contributions to the optical response and can therefore map the carrier distribution profile as a function of both carrier and optical excitation energy. This is plotted in Fig. 4. Here, despite the indirect band gap of each of these materials, hot carriers are predicted to be generated *via* direct transitions almost exclusively. In the MoS_2 profiles, it is clear that indirect excitations of holes to Γ are predicted, although their small overall magnitude suggests they will not contribute significantly to excitation transitions. In both TMDCs, the AB configuration introduces a greater fraction of indirect transitions, however, in both cases the materials are expected to have a majority of direct transitions. Similar behavior has also been experimentally observed in optical studies of bilayer MoS_2 (ref. 51) and WSe_2.[52] In both cases, a substantial contribution to the emission spectra is found to be from direct transitions as opposed to indirect. These experimental results qualitatively agree with the theoretical results found here. Taken altogether, we confirm the preference for direct transitions even for these indirect gap bilayers.

IV. Conclusions

We investigate bilayer TMDCs MoS_2 and WSe_2 *via* an *ab initio* treatment of electron–electron and electron–phonon interactions. Specifically, we describe the complex interplay of spin, layer and valley indexing involved in two different stacking orientations of each bilayer. We find that unlike in the monolayer case, the dynamics are highly TMDC-specific. Based on detailed electronic structure calculations, both electron and hole dynamics (and mobilities) in bilayer WSe_2 are found to be significantly enhanced by spin–orbit coupling in the AB configuration. However, MoS_2 dynamics and mobilities are barely impacted by spin–orbit coupling effects. Stacking orientation was explored and found to be TMDC-specific, as longer lifetimes were found for MoS_2 in the AA′ configuration, compared to the slightly preferred AB configuration in WSe_2. These calculations and results emphasize the significance of understanding the nature of the band edges in determining dynamics, which are highly dependent on interlayer coupling. More generally, these results suggest that effective mechanisms for tuning the orientation and energy of the relevant valleys at the band edges such as layer orientation or strain would be ideal in creating an optimized material for valleytronic application with long-lived states. We also investigate hot carrier generation profiles, which indicate that each of these systems absorb mostly *via* direct transitions, despite their indirect gap nature. The implications of these results are important in understanding bilayers, their spin–valley–layer coupling and relation to symmetry *via* stacking orientation. Understanding coupled spin, valley, layer and symmetry effects in other bilayer $MoSe_2$ and WS_2 will further our understanding of the phenomena observed, and more broadly will help in understanding the underlying nature of quantum material heterostructures and larger multilayer stacks.

Conflicts of interest

There are no conflicts to declare.

Acknowledgements

All authors acknowledge support from the STC Center for Integrated Quantum Materials (CIQM) NSF grant number DMR-1231319 and from the Army Research Office MURI (*Ab Initio* Solid-State Quantum Materials) grant number W911NF-18-1-0431. This work used resources of the National Energy Research Scientific Computing Center, a DOE Office of Science User Facility, as well as resources at the Research Computing Group at Harvard University.

References

1 A. Splendiani, L. Sun, Y. Zhang, T. Li, J. Kim, C.-Y. Chim, G. Galli and F. Wang, *Nano Lett.*, 2010, **10**, 1271.
2 A. M. Jones, H. Yu, N. J. Ghimire, S. Wu, G. Aivazian, J. S. Ross, B. Zhao, J. Yan, D. G. Mandrus, D. Xiao, W. Yao and X. Xu, *Nat. Nanotechnol.*, 2013, **8**, 634.
3 T. Yan, X. Qiao, X. Liu, P. Tan and X. Zhang, *Appl. Phys. Lett.*, 2014, **105**, 101901.
4 K. F. Mak, K. He, J. Shan and T. F. Heinz, *Nat. Nanotechnol.*, 2012, **7**, 494.
5 C. Mai, A. Barrette, Y. Yu, Y. G. Semenov, K. W. Kim, L. Cao and K. Gundogdu, *Nano Lett.*, 2014, **14**, 202.
6 J. R. Schaibley, H. Yu, G. Clark, P. Rivera, J. S. Ross, K. L. Seyler, W. Yao and X. Xu, *Nat. Rev. Mater.*, 2016, **1**, 16055.
7 A. Molina-Sánchez, D. Sangalli, L. Wirtz and A. Marini, *Nano Lett.*, 2017, **17**, 4549.
8 A. K. Geim and I. V. Grigorieva, *Nature*, 2013, **499**, 419.
9 R. Frisenda, E. Navarro-Moratalla, P. Gant, D. P. D. Lara, P. Jarillo-Herrero, R. V. Gorbachev and A. Castellanos-Gomez, *Chem. Soc. Rev.*, 2018, **47**, 53.
10 D. N. Basov, R. D. Averitt and D. Hsieh, *Nat. Mater.*, 2017, **16**, 1077.
11 H. Boschker and J. Mannhart, *Annu. Rev. Condens. Matter Phys.*, 2017, **8**, 145.
12 Y. Cao, V. Fatemi, S. Fang, K. Watanabe, T. Taniguchi, E. Kaxiras and P. Jarillo-Herrero, *Nature*, 2018, **556**, 43.
13 A. Ramasubramaniam, D. Naveh and E. Towe, *Phys. Rev. B: Condens. Matter Mater. Phys.*, 2011, **84**(15), 205325.
14 A. M. van der Zande, J. Kunstmann, A. Chernikov, D. A. Chenet, Y. You, X. Zhang, P. Y. Huang, T. C. Berkelbach, L. Wang, F. Zhang, M. S. Hybertsen, D. A. Muller, D. R. Reichman, T. F. Heinz and J. C. Hone, *Nano Lett.*, 2014, **14**, 3869.
15 Y.-H. Zhao, F. Yang, J. Wang, H. Guo and W. Ji, *Sci. Rep.*, 2015, **5**, 8356.
16 M.-L. Lin, Q.-H. Tan, J.-B. Wu, X.-S. Chen, J.-H. Wang, Y.-H. Pan, X. Zhang, X. Cong, J. Zhang, W. Ji, P.-A. Hu, K.-H. Liu and P.-H. Tan, *ACS Nano*, 2018, **12**, 8770.
17 S. Fang, R. Kuate Defo, S. N. Shirodkar, S. Lieu, G. A. Tritsaris and E. Kaxiras, *Phys. Rev. B: Condens. Matter Mater. Phys.*, 2015, **92**(20), 205108.
18 R. K. Defo, S. Fang, S. N. Shirodkar, G. A. Tritsaris, A. Dimoulas and E. Kaxiras, *Phys. Rev. B*, 2016, **94**, 155310.
19 S. Carr, D. Massatt, S. Fang, P. Cazeaux, M. Luskin and E. Kaxiras, *Phys. Rev. B*, 2017, **95**, 075420.
20 H. Fang, C. Battaglia, C. Carraro, S. Nemsak, B. Ozdol, J. S. Kang, H. A. Bechtel, S. B. Desai, F. Kronast, A. A. Unal, G. Conti, C. Conlon, G. K. Palsson,

M. C. Martin, A. M. Minor, C. S. Fadley, E. Yablonovitch, R. Maboudian and A. Javey, *Proc. Natl. Acad. Sci. U. S. A.*, 2014, **111**, 6198.
21 J. Zhang, H. Hong, J. Zhang, H. Fu, P. You, J. Lischner, K. Liu, E. Kaxiras and S. Meng, *Nano Lett.*, 2018, **18**, 6057.
22 X. Fan, D. J. Singh and W. Zheng, *J. Phys. Chem. Lett.*, 2016, **7**, 2175.
23 J. Kim, C. Jin, B. Chen, H. Cai, T. Zhao, P. Lee, S. Kahn, K. Watanabe, T. Taniguchi, S. Tongay, M. F. Crommie and F. Wang, *Sci. Adv.*, 2017, **3**, e1700518.
24 W. Zhao, Z. Ghorannevis, L. Chu, M. Toh, C. Kloc, P.-H. Tan and G. Eda, *ACS Nano*, 2013, **7**, 791.
25 J. Lee, K. F. Mak and J. Shan, *Nat. Nanotechnol.*, 2016, **11**, 421.
26 S. Wu, J. S. Ross, G.-B. Liu, G. Aivazian, A. Jones, Z. Fei, W. Zhu, D. Xiao, W. Yao, D. Cobden and X. Xu, *Nat. Phys.*, 2013, **9**, 149.
27 B. Zhu, H. Zeng, J. Dai, Z. Gong and X. Cui, *Proc. Natl. Acad. Sci. U. S. A.*, 2014, **111**, 11606.
28 M. Xia, B. Li, K. Yin, G. Capellini, G. Niu, Y. Gong, W. Zhou, P. M. Ajayan and Y.-H. Xie, *ACS Nano*, 2015, **9**, 12246.
29 S. Wang, A. Robertson and J. H. Warner, *Chem. Soc. Rev.*, 2018, **47**, 6764.
30 A. M. Jones, H. Yu, J. S. Ross, P. Klement, N. J. Ghimire, J. Yan, D. G. Mandrus, W. Yao and X. Xu, *Nat. Phys.*, 2014, **10**, 130.
31 S. M. Shinde, K. P. Dhakal, X. Chen, W. S. Yun, J. Lee, H. Kim and J.-H. Ahn, *NPG Asia Mater.*, 2018, **10**, e468.
32 C. J. Ciccarino, T. Christensen, R. Sundararaman and P. Narang, *Nano Lett.*, 2018, **18**(9), 5709–5715.
33 R. Sundararaman, K. Letchworth-Weaver, K. A. Schwarz, D. Gunceler, O. Yalcin and T. Arias, *SoftwareX*, 2017, **6**, 278.
34 J. P. Perdew, A. Ruzsinszky, G. I. Csonka, O. A. Vydrov, G. E. Scuseria, L. A. Constantin, X. Zhou and K. Burke, *Phys. Rev. Lett.*, 2008, **100**, 136406.
35 S. Grimme, *J. Comput. Chem.*, 2006, **27**, 1787.
36 R. Sundararaman and T. A. Arias, *Phys. Rev. B: Condens. Matter Mater. Phys.*, 2013, **87**, 165122.
37 I. Souza, N. Marzari and D. Vanderbilt, *Phys. Rev. B: Condens. Matter Mater. Phys.*, 2001, **65**, 035109.
38 X. Fan, C.-H. Chang, W. T. Zheng, J.-L. Kuo and D. J. Singh, *J. Phys. Chem. C*, 2015, **119**, 10189.
39 Z. Y. Zhu, Y. C. Cheng and U. Schwingenschlögl, *Phys. Rev. B: Condens. Matter Mater. Phys.*, 2011, **84**(15), 153402.
40 F. Ladstädter, U. Hohenester, P. Puschnig and C. Ambrosch-Draxl, *Phys. Rev. B: Condens. Matter Mater. Phys.*, 2004, **70**, 235125.
41 P. Narang, L. Zhao, S. Claybrook and R. Sundararaman, *Adv. Opt. Mater.*, 2017, **5**, 1600914.
42 P. Rivera, J. R. Schaibley, A. M. Jones, J. S. Ross, S. Wu, G. Aivazian, P. Klement, K. Seyler, G. Clark, N. J. Ghimire, J. Yan, D. G. Mandrus, W. Yao and X. Xu, *Nat. Commun.*, 2015, **6**, 6242.
43 A. Srivastava, M. Sidler, A. V. Allain, D. S. Lembke, A. Kis and A. İmamoğlu, *Nat. Nanotechnol.*, 2015, **10**, 491.
44 C. Chakraborty, L. Kinnischtzke, K. M. Goodfellow, R. Beams and A. N. Vamivakas, *Nat. Nanotechnol.*, 2015, **10**, 507.

45 M. Koperski, K. Nogajewski, A. Arora, V. Cherkez, P. Mallet, J.-Y. Veuillen, J. Marcus, P. Kossacki and M. Potemski, *Nat. Nanotechnol.*, 2015, **10**, 503.
46 C. Chakraborty, K. M. Goodfellow and A. Nick Vamivakas, *Opt. Mater. Express*, 2016, **6**, 2081.
47 C. Chakraborty, K. M. Goodfellow, S. Dhara, A. Yoshimura, V. Meunier and N. Vamivakas, *Nano Lett.*, 2017, **17**, 2253.
48 C. Chakraborty, L. Qiu, K. Konthasinghe, A. Mukherjee, S. Dhara and N. Vamivakas, *Nano Lett.*, 2018, **18**, 2859.
49 R. Sundararaman, P. Narang, A. S. Jermyn, W. A. Goddard III and H. A. Atwater, *Nat. Commun.*, 2014, **5**, 5788.
50 A. M. Brown, R. Sundararaman, P. Narang, W. A. Goddard and H. A. Atwater, *ACS Nano*, 2016, **10**, 957.
51 A. K. M. Newaz, D. Prasai, J. I. Ziegler, D. Caudel, S. Robinson, R. F. Haglund Jr and K. I. Bolotin, *Solid State Commun.*, 2013, **155**, 49.
52 H. Zeng, G.-B. Liu, J. Dai, Y. Yan, B. Zhu, R. He, L. Xie, S. Xu, X. Chen, W. Yao and X. Cui, *Sci. Rep.*, 2013, **3**, 1608.

